Hydrodynamic resistance and mobility of deformable objects in microfluidic channels

P. Sajeesh, M. Doble, and A. K. Sen[a)]
Department of Mechanical Engineering, Indian Institute of Technology Madras, Chennai-600036, India and Department of Biotechnology, Indian Institute of Technology Madras, Chennai-600036, India

(Received 28 May 2014; accepted 25 September 2014; published online 6 October 2014)

This work reports experimental and theoretical studies of hydrodynamic behaviour of deformable objects such as droplets and cells in a microchannel. Effects of mechanical properties including size and viscosity of these objects on their deformability, mobility, and induced hydrodynamic resistance are investigated. The experimental results revealed that the deformability of droplets, which is quantified in terms of deformability index (D.I.), depends on the droplet-to-channel size ratio ρ and droplet-to-medium viscosity ratio λ. Using a large set of experimental data, for the first time, we provide a mathematical formula that correlates induced hydrodynamic resistance of a single droplet ΔR_d with the droplet size ρ and viscosity λ. A simple theoretical model is developed to obtain closed form expressions for droplet mobility ϕ and ΔR_d. The predictions of the theoretical model successfully confront the experimental results in terms of the droplet mobility ϕ and induced hydrodynamic resistance ΔR_d. Numerical simulations are carried out using volume-of-fluid model to predict droplet generation and deformation of droplets of different size ratio ρ and viscosity ratio λ, which compare well with that obtained from the experiments. In a novel effort, we performed experiments to measure the bulk induced hydrodynamic resistance ΔR of different biological cells (yeast, L6, and HEK 293). The results reveal that the bulk induced hydrodynamic resistance ΔR is related to the cell concentration and apparent viscosity of the cells. © *2014 AIP Publishing LLC*.
[http://dx.doi.org/10.1063/1.4897332]

I. INTRODUCTION

The area of microfluidics deals with development of miniaturized fluidic devices (with channel size ~1–1000 μm) that has undergone impressive advancements during the last two decades.[1–6] As an interdisciplinary area, this technology has profound applications in biomedical diagnostics, chemical and biological analysis,[7–9] automotive, and electronics industries. One of the pivotal applications of microfluidics is the development of lab on chip (LOC) devices. LOC devices that enable sorting of micron-sized objects such as cells, droplets, and particles into distinct populations could be a powerful tool in a range of applications including healthcare, research, and industry. Ability to sort cells based on size and deformability can provide an indispensable diagnostic tool.[10–12] Recently, induced hydrodynamic resistance (i.e., the additional resistance due to the presence of an object in a microchannel flow) has been proposed as a parameter for characterization of such objects.[13] Hydrodynamic resistance is related to the mechanical properties of objects including size and deformability. Based on the induced hydrodynamic resistance, objects of different mechanical properties could be sorted.[14] Thus, investigation of induced hydrodynamic resistance and overall dynamics of deformable objects in a microfluidic channel has great practical significance.

[a)]Author to whom correspondence should be addressed. Electronic mail: ashis@iitm.ac.in

Excess pressure drop and mobility of droplets (i.e., ratio of velocity of droplet to the total velocity of continuous phase) in a rectangular channel has been studied for droplets of different size and viscosity ratio.[15,16] Excess pressure drop produced by a single droplet in a rectangular channel was also investigated using a sensitive microfluidic comparator.[17] In the case of small droplets of length less than 4-times the channel width, pressure drop is independent of drop size and weakly dependent on the viscosity ratio. For larger droplets, excess pressure drop may increase, decrease, or remain unchanged with drop size depending on the viscosity ratio.[17] Engl *et al.*[18] performed experiments with a train of droplets in a millifluidic channel and designed a channel network for routing of droplets based on the induced hydrodynamic resistance. Labrot *et al.*[19] carried out experiments to determine the hydrodynamic resistance offered by liquid plugs in a microchannel using a pressure sensor as well as an asymmetric loop device. Effect of surfactant adsorption at the droplet interface leads to a reduction in droplet velocity, and this retardation increases with increase in droplet size ratio and decrease in viscosity ratio.[20] Also, presence of surfactant increases the leading end curvature of the droplet interface, which has significant effect on droplet speed and excess pressure drop. At low Peclet number (ratio of surfactant convection to the two dimensional diffusion at the interface), diffusion become dominant and surfactant concentration is uniform which leads to lower surface tension. At high Peclet number, surfactant gradient produces Marangoni stresses leading to surface immobilization thus increasing excess pressure drop and decreasing droplet velocity. Fuerstman *et al.*[21] studied excess pressure drop produced when a large bubble contacts all four walls of a rectangular microchannel. It was observed that at low and high surfactant concentrations, pressure drop mainly depends on the number of bubbles in the channel. At intermediate surfactant concentrations, pressure drop depends on the total aggregated length of the bubbles. In the latter case, there is an increased flow of continuous phase through the region bounded by the curved surface of the bubble and the corners of the channel which is known as "gutter effect." Excess pressure drop produced by a single droplet inside a channel in terms of an equivalent hydrodynamic length was calculated from experiments and model.[22]

Although, recently, some efforts have been made to understand the hydrodynamics of micron size deformable objects in microchannels, there are several limitations. In the numerical studies reported in literature, the contact angle made by discrete phase has been approximated as the wetting boundary condition at the wall, whereas it is actually the angle made by the interface with the channel wall measured along the denser liquid phase. At microscale, surface tension force is predominant due to which contact angle has significant effect on the droplet production, diameter, frequency, mobility, and deformation. Thus, in the Volume-of-Fluid (VOF) simulations, it is important that a correct value of contact angle is specified in the boundary conditions. Initial studies on excess pressure drop of droplets were made in circular channels which considered the droplets to be less deformable and inviscid.[23] Most of the analytical and numerical models reported in literature[24] address the mobility of isolated rigid spherical objects and fluid spheres with high surface tension in vertical capillaries with or without consideration of the effect of gravity. In these models, deformation of these spherical objects is not considered. Also, most of the models fail to accurately predict the mobility of droplets of diameters above 0.8 times the channel size. Some experimental and numerical works[25] considered deformability of neutrally buoyant droplets to determine mobility and excess pressure drop but these studies were carried out inside macro-scale channels (where scaling of forces may be different). In contrast to the observations made earlier,[23,26] recent studies[27] have shown that the hydraulic resistance increases with increase in droplet size irrespective of the viscosity ratio (i.e., even if it is less than 0.48). It is reported that this contradictory observations could be due to neglect of the pressure exerted by thin film of the continuous phase around the droplet in the previous model. Droplets having different density as compared to the continuous phase have been studied[28] but these studies were for large droplets inside tubes. Recently, hydrodynamic resistance induced by a single droplet in small channels is studied using analytical models and experiments,[29] but these models do not address the effect of viscosity ratio or droplet deformability. Another recent work[19] does consider the effect of viscosity ratio of droplets but these studies were performed using liquid plugs. Additionally, although some research has been

carried out to study the effective viscosity, flow pattern, and distribution of particles, such as beads and cells inside narrow confinements,[29,30] only limited studies[31] have been performed to investigate the effect of concentration of such microparticles on the induced hydrodynamic resistance.

This paper reports hydrodynamic behaviour including deformation, mobility, and induced hydrodynamic resistance of micron size deformable objects (droplets, beads, and cells) of different mechanical properties (size and viscosity) inside rectangular microchannels. The first part of the paper presents a theoretical model to predict droplet mobility and induced hydrodynamic resistance of droplets moving in a microfluidic channel. Sessoms *et al.*[22] reported a phenomenological model for predicting equivalent hydrodynamic length and mobility of a single droplet in a microchannel. Our theoretical model is an extension of this work which facilitates experimental measurement of the phenomenological permeability, which[22] does not attempt. Additionally, our model reduces the number of such permeabilities from three to one by (a) considering the flow in the annular region around the droplet and (b) considering the Poiseuille flow profile in the unobstructed region. Next, a numerical model is outlined which is used to simulate droplet generation and deformation behaviour of droplets of different size and viscosity. Further, the device fabrication protocol, experimental setup, materials and methods for droplets and bead/cell samples, and characterization of chemicals used in the experiments are detailed. Then, the results of the analytical model, numerical simulations, and experiments for the droplets are presented and discussed. Effect of droplet size and viscosity ratio on the deformation pattern, mobility, and induced hydrodynamic resistance are reported. Finally, experimental results for polystyrene microbeads and cells (Yeast, L6 myoblast, and HEK-293) are presented and discussed.

II. THEORETICAL MODEL

In this section, induced hydrodynamic resistance (ΔR_d) and mobility (ϕ) of individual droplets present in a microfluidic channel are derived. Presence of a droplet inside a microfluidic channel increases the hydrodynamic resistance of the channel. If $\Delta R_{wd} = \Delta P_{wd}/Q$ and $\Delta R_{wod} = \Delta P_{wod}/Q$ are the hydrodynamic resistances of the channel with and without the presence of droplets, respectively, the "induced hydrodynamic resistance" due to a single droplet is given by $\Delta R_d = (\Delta R_{wd} - \Delta R_{wod})/n$. Here, ΔP_{wd} and ΔP_{wod} are pressure drops with and without droplets, respectively, Q is the total flow rate and n is the total number of droplets. The presence of a droplet is also represented by a parameter called "equivalent hydrodynamic length L_d," which is the additional length of the channel required to match the additional pressure drop due to a single droplet, while operating with the continuous phase only and the same total flow rate. First, an expression for droplet mobility ϕ, which is the ratio of the velocity of the droplet U_d to the average velocity of the continuous phase U_T, is derived. Next, an expression for equivalent hydrodynamic length of a droplet is derived and then expression for induced hydrodynamic resistance of a droplet is obtained.

Consider a microchannel having uniform cross-section of hydraulic radius R_c and length L with n is the number of equispaced monodisperse droplets of radius R_d, density ρ_d, and viscosity μ_d moving at velocity U_d as depicted in Fig. 1. The density and viscosity of continuous phase are ρ_c and μ_c, respectively. Let the separation distance between the droplets be δ. Due to

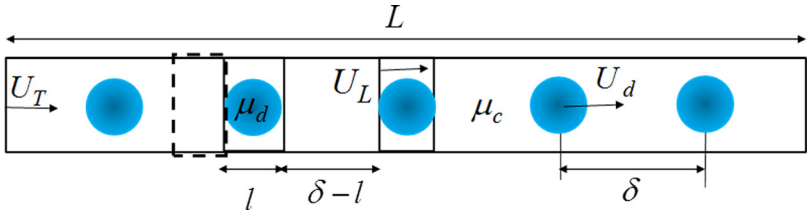

FIG. 1. Schematic of the model showing homogeneous equispaced (interdistance δ) droplets in a microchannel of length L and the regions with droplets (l) and without droplets ($\delta - l$).

the periodic nature of the droplets, flow in a channel portion of length δ is considered. If δ is sufficiently large such that there is no hydrodynamic interaction between the droplets, it can be assumed that a droplet modifies the original Poiseuille flow field only over a small segment of length $l < \delta$. It is expected that the maximum value of l can be of the order of the size of the channel R_c. With these considerations, the flow inside the microchannel can be divided into two distinct regions, viz., a region of length l which is affected by the presence of the droplet and the interdroplet region of length $\delta - l$ which is unperturbed and exhibits Poiseuille flow. Let the average velocity of continuous phase in the unperturbed region $(\delta - l)$ be U_T and velocity of continuous phase in the annular region around the droplet is U_L.

First, an expression for the velocity profile of the fluid in the annular region is derived by considering the movement of a cylindrical droplet inside a cylindrical channel. As explained further in Sec. V A, moving droplets of size comparable to that of the channel size take the shape of a bullet or capsule (prolate profile). So, the approximation of a cylinder moving inside another stationary cylinder can be considered to determine the modified velocity in the annular region. Under the assumption of fully developed flow and negligible body force, Navier-Stokes equation for an incompressible flow in the annular axisymmetric region around the droplet is given by

$$\frac{1}{r}\frac{\partial}{\partial r}\left(r\,\frac{\partial u}{\partial r}\right) = -\frac{1}{\mu_C}\left(\frac{\partial p}{\partial z}\right), \tag{1}$$

where p is fluid pressure, u is flow velocity, and r and z are radial and axial coordinates, respectively. By integrating and applying the following boundary conditions: $r = R_d$, $u = U_d$(droplet velocity) and $r = R_c$, $u = 0$ (no-slip on channel wall), the velocity profile in the annular region is derived as

$$u(r) = \frac{1}{4\mu_c}\frac{\Delta P_l}{l}\left(R_c^2 - r^2\right) + \left(\frac{U_d - \frac{1}{4\mu_c}\frac{\Delta P_l}{l}\left(R_c^2 - {R_d}^2\right)}{\ln\frac{R_c}{R_d}}\right)\ln\left(\frac{r}{R_c}\right), \tag{2}$$

where ΔP_l is the pressure drop in the region affected by the presence of the droplet. The expression for average velocity of continuous phase in the annular region is calculated as

$$U_L = \frac{1}{\pi\left(R_c^2 - R_d^2\right)}\int_{R_d}^{R_c} u(r)\,2\pi r\,dr, \tag{3}$$

$$U_L = \frac{1}{8\mu_c}\frac{\Delta P_l}{l}\left(R_c^2 - {R_d}^2\right) + \left(\frac{U_d - \frac{1}{4\mu_c}\frac{\Delta P_l}{l}\left(R_c^2 - {R_d}^2\right)}{\ln\left(\frac{R_d}{R_c}\right)}\right)\left(\frac{R_d^2\ln\left(\frac{R_c}{R_d}\right)}{\left(R_c^2 - {R_d}^2\right)} - \frac{1}{2}\right). \tag{4}$$

In the droplet region, continuous phase is modified due to the presence of the droplet. Assuming that Darcy's laws hold true around the droplet in region l (i.e., velocity of a fluid element is proportional to the pressure drop applied across it,[22,32] we get

$$\frac{\Delta P_l}{l} = \frac{\mu_c}{k_d}U_T, \tag{5}$$

where k_d is the permeability of the medium around the droplet, which depends on the ratio of the droplet size to the channel size (ρ) and the discrete-to-continuous phase viscosity ratio (λ). The expression for k_d is determined using a large set of experimental data as discussed later in Sec. V C.

In flows through porous media, to satisfy continuity, the interstitial velocity at the porous region and the superficial velocity in the nonporous region are related by porosity or void fraction.[32] The continuous phase velocity U_T and the velocity of flow in the annular region around the droplet U_L are analogous to the superficial velocity and the interstitial velocity, respectively. Thus,

$$U_L = \frac{U_T}{\varepsilon}, \tag{6}$$

where ε is the porosity of the region l, which is the volume fraction of continuous phase in this region l. If the volume of the region l is V_l and the volume of the droplet is V_d, the volume of the void region around the droplet can be calculated as $V_c = V_l - V_d$, which can be used to calculate the porosity as $\varepsilon = V_c/V_l$.

Using Eq. (6) in Eq. (5), we get

$$\frac{\Delta P_l}{l} = \frac{\mu_c}{k_d}\varepsilon U_L. \tag{7}$$

Substituting Eq. (6) in Eq. (4), we get $U_L = TU_D$, where

$$T = \frac{\dfrac{R_d^2}{\left(R_c^2 - {R_d}^2\right)} + \dfrac{1}{2\ln\left(\dfrac{R_d}{R_c}\right)}}{\dfrac{\varepsilon\left(R_c^2 - {R_d}^2\right)}{8k_d} + \dfrac{\varepsilon {R_d}^2}{4k_d} + \dfrac{\varepsilon\left(R_c^2 - {R_d}^2\right)}{8k_d\ln\left(\dfrac{R_d}{R_c}\right)} - 1}. \tag{8}$$

Considering a control volume in the region $\delta - l$ (shown by dotted line in Fig. 1), which is bounded by the channel walls as the top and bottom faces, a channel cross-section in the unobstructed region as the left face and a channel cross-section on the trailing edge of a droplet as the right face, mass conservation yields

$$A_T U_T = A_L U_L + A_D U_d. \tag{9}$$

Substituting $U_L = TU_d$, the non-dimensional droplet velocity or droplet mobility ϕ can be expressed as

$$\phi = \frac{U_d}{U_T} = \frac{1}{\dfrac{A_L}{A_T}T + \dfrac{A_D}{A_T}}, \tag{10}$$

where A_L is the annular area around the droplet in region l, A_D is the cross sectional area of the droplet, and A_T is the cross sectional area of the channel. The pressure drop over a channel segment of length δ can be obtained by adding the individual pressure drops in the two regions as

$$\Delta P_\delta = \Delta P_l + \Delta P_{\delta - l}. \tag{11}$$

The pressure drop ΔP_l is given by Eq. (5) and the pressure drop in the region $(\delta - l)$ is given by

$$\Delta P_{(\delta - l)} = \frac{8\mu_C U_T(\delta - l)}{R_C^2}. \tag{12}$$

Substituting Eqs. (5) and (12) in Eq. (11) and rearranging the terms, we get

$$\Delta P_\delta = \frac{\mu_c}{k_d}U_T l + \frac{8\mu_c U_T}{R_c^2}(\delta - l). \tag{13}$$

Considering that the pressure drop over a length L of the channel is given by $\Delta P_{wd} = (L/\delta)\Delta P_\delta$ and the number of droplets $n = L/\delta$, the excess pressure drop can be obtained as

$$\Delta P_{excess} = (L/\delta)\Delta P_\delta - \frac{8\mu_c U_T L}{R_c^2} = \frac{nlU_T\mu_c}{R_c^2}\left(\frac{R_c^2}{k_d} - 8\right). \tag{14}$$

So, the equivalent hydrodynamic length of a single droplet can be expressed as

$$L_d = l\left(\frac{R_c^2}{8k_d} - 1\right) = l\left(\frac{1}{k_d^*} - 1\right) \tag{15}$$

and the induced hydrodynamic resistance due to a single droplet is obtained as

$$\Delta R_d = \frac{8\mu_c l}{\pi R_c^4}\left(\frac{1}{8k_d^*} - 1\right), \tag{16}$$

where $k_d^* = k_d/R_c^2$ is the dimensionless permeability. It is observed that the induced hydrodynamic resistance ΔR_d depends on the size of the droplet and the channel as well as the viscosity of the carrier fluid and droplet (via k_d). Further, if we non-dimensionalize ΔR_d using hydrodynamic resistance (R) offered by the continuous phase alone operated at the same total flow rate, we get

$$\frac{\Delta R_d}{R} = \frac{l}{L}\left(\frac{1}{8k_d^*} - 1\right). \tag{17}$$

III. NUMERICAL MODEL

Numerical simulations are carried out using VOF model in Ansys-Fluent. Assuming that fluid is Newtonian and flow is incompressible, laminar and fully developed, the governing equations for mass, momentum, and fluid fraction function are as follows:

$$\nabla . u = 0, \tag{18}$$

$$\frac{\partial \rho u}{\partial t} + \nabla . \rho u u = -\nabla P + \nabla . \left(\mu(\nabla u + \nabla^T u)\right) + F_s, \tag{19}$$

$$\frac{\partial F}{\partial t} + u . \nabla F = 0, \tag{20}$$

where u is the flow velocity, p is the pressure shared by two phases, and F is the volume fraction in a cell that ranges between 0 and 1. For a cell that is completely filled with secondary phase (droplet phase), $F = 1$, whereas for a cell that is completely filled with the primary phase (continuous phase) $F = 0$. If a cell contains an interface between two phases, the phase fraction has an intermediate value between 0 and 1. All the physical properties including density ρ and viscosity μ used in the equations are the averaged by volume fraction of individual phases, and F_s is the surface tension force which is added to the momentum equation as a source term.

In VOF method, surface tension force is calculated by using continuum surface force model,[33] where the surface curvature is computed from the local gradients in the surface normal at the interface. The gravitational force is neglected as it is not relevant in case of micro-scale flows. The interfacial tension and material properties used in the simulations are measured from our experiments (presented in Table I). Velocity boundary conditions are applied at the inlets of the discrete and continuous phases and atmospheric pressure boundary condition is used at the outlets. One-half of the computational domain is simulated with a symmetry boundary condition to reduce computational time. Wetting effect of the fluid on the wall is handled by

TABLE I. Properties of DI water + glycerol % (wt/wt) and mineral oil + 5% Span 85 (wt/wt) measured at 24 °C.

Chemical	Viscosity (Pa s)	Density (Kg/m^3)	Surface tension (mN/m)	Interfacial tension with mineral oil + span 85 (5% wt/wt) (mN/m)	Contact angle (°)
DI water + 0% glycerol	0.000914	994	72.51	3.501	96.91 ± 1.16
DI water + 20% glycerol	0.001564	1040	70.48	3.216	76.66 ± 0.6
DI water + 40% glycerol	0.003237	1097	69.14	3.109	92.3 ± 2.69
DI water + 60% glycerol	0.0086	1155	67.74	3.012	94.04 ± 3.27
DI water + 80% glycerol	0.0421	1207	66.83	2.931	100.78 ± 2.11
Mineral oil + 5% Span 85 wt/wt	0.0287	857	27.22	…	43.92 ± 2.98

providing a static contact angle as wall boundary condition. The contact angle is measured from the experimental images captured using a high speed camera and analysed using ImageJ software. Pressure Implicit with Split of Operators (PISO) is used as the pressure-velocity coupling scheme and Pressure Staggering Option (PRESTO) is used as the pressure interpolation scheme for calculating the face pressure of each cell.

We use two-dimensional (2D) simulations to predict the droplet generation process. In the case of small surface tension (high *Ca*) unconfined extensional flows, droplet formation is attributed to the capillary (i.e., Rayleigh–Plateau) instability. This capillary instability is not operative in two dimensions and thus cannot be simulated by a 2D code.[34] However, this is not the situation in our case because we are operating at low to moderate *Ca* in the range 0.01–0.2, where the droplet formation is caused by an increased upstream pressure due to lubrication flow in a thin film sandwiched between the droplet and the channel wall.[35] We simulate the droplet formation using Fluent code which employs inbuilt Brackbill continuum surface tension model[33] to represent the above mechanism and cause the droplet formation. In our initial simulations, we had performed 3D simulations to predict droplet formation. We found that the 3D simulations are computationally very expensive but do not provide any considerable improvement in accuracy as compared 2D simulations. Moreover, most of the numerical works on droplet break up using flow focusing geometry reported in literature[34,36] are performed on a 2D code.

For simulating droplet generation process, explicit scheme is used for time step discritization and second order upwind scheme is used for spatial discretization of the momentum equation. The interface reconstruction is done using geometric reconstruction scheme (piece wise linear approach) to determine the volume fraction weighted average density and viscosity for the cells and to interpolate face flux for the convective terms in the governing equations. Grid and time-step independence studies were performed by considering the interface diffusion and droplet diameter and the required number of grids and time-step were determined to be 15 789 and 1 μs. In order to predict the effect of size and viscosity on droplet deformation, three-dimensional (3D) VOF simulations are required. Implicit scheme is used for the time step discritization and second order upwind scheme is used for the volume fraction discritization. Grid and time-step independence studies were performed and the required number of grids and time-step was found to be 1 40 976 and 1 μs. Droplets of different size were defined inside a microchannel by adapting the mesh inside the droplets as the secondary phase. Parasitic currents, which leads to cumulative error in simulation, were eliminated by smoothening the volume fraction near the interface by adapting more elements (mesh refinement) close to the interface.

IV. EXPERIMENTS

A. Device fabrication

The microchannel devices used in the present studies were fabricated in PDMS by using standard soft lithography procedures. A flexi mask designed in AutoCAD LT 2008 was printed

at 40 000 dpi. (Photozone Graphics, Mumbai, India). To ensure rigidity of the mask during photolithography, the mask was fixed onto a thin glass plate. A 4″ silicon wafer (Semiconductor Technology and Application, Milpitas, USA) used for photolithography was cleaned (using RCA1, RCA2, and HF dip followed by DI water rinse) and placed in oven for 2 min at 120 °C to remove moisture. First, a very thin layer of 1,1,1,3,3,3 Hexamethyldisilazane (HMDS) (Spectrochem Pvt. Ltd., Mumbai, India) was spun coated onto the wafer to improve adhesion between photoresist and wafer. Photoresist SU8 2075 (MicroChem Corp, Newton, USA) was spun coated onto the wafer at 2000 rpm for 30 s with an acceleration of 300 rpm/s. Soft baking was done at 65 °C for 5 min followed by 95 °C for 10 min. The photoresist was exposed to UV light (J500-IR/VISIBLE, OAI Mask alligner, CA, USA) through the mask for 30 s. Post exposure bake was done at 65 °C for 2 min followed by 95 °C for 8 min. Then, the UV-exposed wafer was developed to obtain the silicon master with SU8 pattern on top of it, which was placed in oven at 100 °C for 30 min to further improve adhesion between photoresist and wafer.

PDMS monomer and curing agent (Sylgard- 184, Silicone Elastomer kit, Dow Corning, USA) were mixed at a ratio of 10:1 by weight, and the mixture was degassed in a desiccators to remove air bubbles trapped during mixing. PDMS was poured onto the silicon master, which was then cured inside a vacuum oven at 75 °C for 4 h. After curing, the hardened PDMS layer containing the channel structure was peeled off the silicon master and cut to size. Fluidic access holes for the inlet/outlet and the pressure taps were punched using a 1.5 mm biopsy punch (Shoney scientific, Pondicherry, India). The PDMS layer containing the microchannel structure was bonded to a glass slide using an oxygen plasma bonder (Harrick Plasma, Brindley St., USA). Finally, PTFE tubings (Cheminert fittings-VICI, Germany) were glued to the access holes to establish fluidic connection. A photograph of the chip, a zoomed view of the droplet junction and SEM image of the channel cross-section are depicted in Figs. 2(a)–2(c), respectively. The hydraulic diameter of the channel cross-section is measured to be 97.58 μm.

B. Materials and methods

1. Droplets

In our experiments with droplets, mineral oil (Sigma Aldrich, Bangalore, India) was used as continuous phase and water + aqueous glycerol (Sigma Aldrich, Bangalore, India) with concentration of glycerol in the range 20%–80% wt/wt was used as discrete phase. The concentration of glycerol controls the viscosity of the discrete phase. Surfactant was added to the mineral oil to improve stability of the aqueous droplets and hydrophobicity of the channel, which in turn helps in achieving repeatability of droplet production. To generate aqueous droplets in oil, a lipophilic surfactant having a Hydrophilic-Lipophilic Balance (HLB) number in the range 1–6 should be added to the oil phase.[37] In our experiments, Span 85 (Sigma Aldrich, Bangalore, India) having HLB number of 1.8 was used, which is soluble in mineral oil but insoluble in the aqueous phase. The interfacial tension of mineral oil decreases with increase in surfactant concentration, and the achievable lower limit of the surface tension is imposed by the surfactant solubility limit. If the concentration of surfactant is above the surfactant solubility limit, interfacial tension remains constant.[38] At such high concentrations, surfactants start to form micelles, so this concentration is called "Critical Micelles Concentration (CMC)." When the surfactant

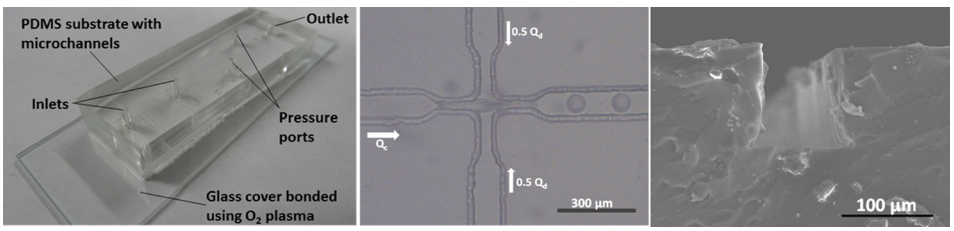

FIG. 2. (a) Photograph of the microchannel device, (b) zoomed view of the droplet junction and (c) SEM image of the microchannel.

concentration is less than the CMC, the surfactants are unevenly distributed over the interface, which produces a concentration gradient over the droplet surface. This leads to the Marangoni stresses in addition to the already existing tangential and normal stresses acting on the surface of the droplet. If the concentration is well above CMC, added excess surfactant form micelles and thus concentration of individual surfactant molecules over the droplet surface is constant and is equal to the CMC. Thus, Marangoni stress over the surface is avoided which helps in the production of stable droplets.

The effect of Span 85 on interfacial tension was studied recently.[39] It is reported that for most of the non-ionic surfactants, the CMC value is in the range of 1.2×10^{-4}–7.6×10^{-4} mol/dm^3. Previous studies have shown that CMC value of Span 85 in mineral oil is 0.262% wt/volume (or 0.003% wt/wt). We performed experiments to study the effect of concentration of Span 85 (in mineral oil) on the size of droplets produced by varying the concentration in the range of 0.5%–10% wt/wt. It was observed that the diameter of the droplets decreased (e.g., diameter decreases from 123 μm to 99 μm at a flow rate of 4.1 μl/min) with increase in the surfactant concentration up to 5% wt/wt and above this; the sizes of the droplets remain constant. It was observed that a high surfactant concentration ($\sim$10%) leads to the formation of pilot droplets thus preventing a uniform droplet size distribution, which is required in the present study. In our experiments with droplets, we have used a surfactant concentration of 5% wt/wt in order to achieve uniform and stable droplets. The interfacial tension between mineral oil and the aqueous phase (at different glycerol concentrations) was measured by Du Nouy ring method using a Tensiometer (Sigma 701 Tensiometer, Sweden). Without addition of any surfactant, the interfacial tension between mineral oil and DI water (Milli Q) was measured to be 52.5 mN/m. With 5% wt/wt Span 85, the interfacial tension was measured to be 3.501 mN/m. Viscosity measurements were carried out using a viscometer (Brook field DV-II + Pro Extra, USA) and contact angle measurements on PDMS substrates were carried out using Goniometer (Holmarc Opto-Mechatronics Pvt. Ltd., India). The measurement results for viscosity, density, surface tension, contact angle, and interfacial tension are summarized in Table I. These values are used in the numerical simulations and calculations of the results of theoretical model and experiments.

2. Microbeads

In our experiments with microbeads, polystyrene beads (Sigma Aldrich, Bangalore, India) of 10 μm size were suspended in 22% aqueous glycerol. The density of aqueous glycerol is same as that of the beads; thus, sedimentation of beads during the experiments was prevented. The mixed sample was added with 0.5% wt of Tween 85 (Sigma Aldrich, Bangalore, India) to prevent aggregation of beads. The number of particles in 1 ml of original bead sample (from vendor) was calculated as follows:

$$N_p = \frac{6 \times 10^{10}(W_V\%)}{\pi \rho_p D^3}, \tag{21}$$

where $W_V\%$ is the percentage latex concentration in g/100 ml of original bead sample, ρ_p is the density of polystyrene, and D is the diameter of beads. Finally, the original bead sample was diluted with aqueous glycerol (22%) to achieve different bead concentrations (0.9, 1.8, 2.71, 4.52, 6.33, and 9.05×10^5 beads/ml).

3. Yeast

In our experiments with yeast cells, *Saccharomyces cerevisiae* MTCC 3090 were purchased from Institute of Microbial Technology (MTCC) Chandigarh, India. The cells were cultured in Yeast Extract Peptone Dextrose (YEPD) medium for 48 h at 30 °C. The number of cells was determined by measuring the optical density (OD) at 600 nm with a UV- Visible Spectrophotometer (Jasco V-550, Japan). The culture was grown to reach an optical density of 1.0 (1.0 is approximately equal to 1×10^7 cells/ml, which is confirmed by hemocytometer

(Marienfeld, Germany).[40] The yeast cells were then diluted with YEPD to achieve different cell concentrations (0.25, 0.5, 1.0, 1.5, 2.0, and 2.5×10^5 cells/ml).

4. Cells (L6 myoblast and HEK 293)

In our experiments with cells, L6 myoblast cells and Human Embryonic Kidney 293 cells (HEK 293) were purchased from NCCS (National Centre for Cell Sciences) Pune, India. The cells were grown to confluence in Dulbecco's Modified Eagle Medium (DMEM) (Himedia, India), which contained 10% fetal bovine serum and antibiotic mix (50 mg gentamicin, 100 mg streptomycin, and 62.77 mg penicillin).[41] The medium from the confluent cells were removed and the cells were washed thrice with Phosphate Buffered Saline (PBS). Then, PBS was removed completely and trypsinized with 1× trypsin (3 min incubation in 5% CO_2 incubator). The trypsinized cells were added with 1 ml DMEM and centrifuged for 5 min at 1800 rpm. The supernatant was removed and 1 ml of medium was added to the pellet and gently mixed. The number of cells was counted with the help of a haemocytometer (Marienfeld, Germany).[42] They were then diluted with DMEM to achieve different cell concentrations (0.25, 0.5, 1.0, 1.5, 2.0, and 2.5×10^5 cells/ml).

C. Experimental setup and procedure

A schematic and photograph of the experimental setup are shown in Fig. 3. The microchannel device includes a droplet generator with a cross-junction. Mineral oil (with surfactant) and aqueous glycerol are filtered using a 13 mm, 0.2 μm pore size PTFE, and nylon syringe filters, respectively (Axiva Sichem Biotech, Chennai, India). All the experiments were performed using 2 ml, 1000 series gas tight glass syringes (Hamilton Company, Nevada, USA). These gas-tight glass syringes provide quicker response and low pressure fluctuations as compared to plastic syringes. Mineral oil as the continuous phase and aqueous glycerol as discrete phase are supplied using syringe pumps (TSE systems, Germany). Pressure drop measurements are performed using a PX26–005DV differential pressure sensor with a DP25B S-230A display unit (Omega, Stanford, USA), which is capable of measuring transient pressure (with response time ~1 ms) across the pressure taps. The capillaries connecting the pressure taps on the device and the pressure sensor are primed carefully to avoid possibility of oil-air interface inside that may influence the reading. Our test section (between the pressure taps) is located sufficiently away (at 2.5 cm) from the droplet generation junction to ensure that the droplets are focused at the centre before entering the test section.[43,44]

From our preliminary experiments, it was observed that the wetting behaviour of microchannels get modified significantly as time progresses. So, the repeatability of the experiments was poor even after providing a hydrophobic Octadecyltrichlorosilane coating (OTS) on the channel. The channels acquire a steady wetting behaviour (hydrophobicity) 1–2 weeks after fabrication (plasma exposure). So, all the experiments were performed after 2-weeks of fabrication. The experiments were performed inside an air-conditioned laboratory environment at a temperature of 24 °C to eliminate the influence of temperature on the viscosity of the aqueous glycerol (which is highly sensitive to temperature change even at ±0.5 °C). First, the entire channel was flushed with mineral oil (with surfactant) to ensure uniform wetting of the channel. Then,

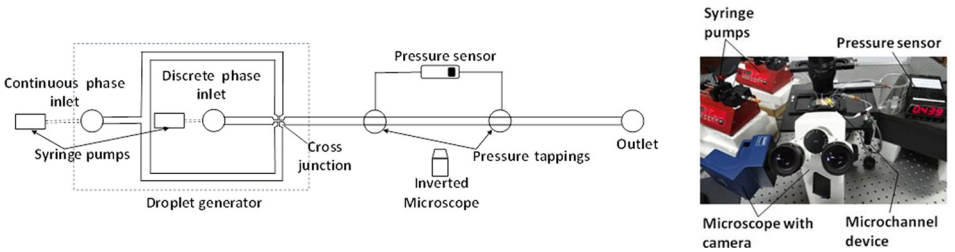

FIG. 3. Schematic (left) and photograph (right) of the experimental setup used for pressure drop measurement.

discrete phase was introduced into the device to generate droplets at the cross-junction. The pressure drop was continuously monitored using the pressure sensor after steady state was reached after 3–5 min. The flow rates of both continuous and discrete phases were adjusted individually to achieve stable monodispersed droplets with equal interdistance between them. The size and shape of the droplets and the separation distance between them were measured using an inverted microscope (Carl Zeiss Axiovert A1) coupled with a CCD camera (ProgRes CF Cool, Jenoptik, Germany) interfaced with PC via ProgRes CapturePro v2.8.8 software. As the droplets moving inside the channel having bullet shape, the diameter of the droplets is measured inside a larger fluidic port at the channel exit, where the droplets attain spherical shape.

In the experiments with microbeads and cells, the samples were infused into the device through the continuous phase inlet of the chip (Fig. 2) and the other inlet port (discrete phase inlet) was sealed. Before the experiments, the channel and the pressure senor ports were flushed with the medium fluid (aqueous glycerol in case of bead experiments and PBS in case of cell experiments) in order to avoid any contamination. With the beads/cells flowing through the test section (between the pressure taps in Fig. 2), pressure drop was recorded using the pressure sensor described earlier. In order to measure the pressure drop of the media only (without any beads/cells), the cells and beads were removed from the media by centrifugation (5 min in a centrifuge Remi-R-8C, Remi Elektrotechnik Limited, India) and filtration (using filter described earlier), respectively.

V. RESULTS AND DISCUSSION

A. Droplet size and deformation

Droplets of aqueous glycerol (i.e., water + glycerol 0%–80%) were generated in mineral oil (with surfactant Span 85 at 5% wt/wt). Initially, experiments were performed to identify the operating conditions for generating monodisperse droplets with equal interdistance between them, for all aqueous glycerol compositions. Droplets of different size were generated by varying the total flow rate Q_T, for various aqueous glycerol compositions. The total flow rate Q_T was varied by adjusting both continuous phase flow rate Q_c and discrete phase flow rate Q_d while keeping the flow rate ratio Q_c/Q_d fixed. It was observed that the droplet diameter D_d is reduced with increase in the total flow rate Q_T, for all viscosity ratios $\lambda = \mu_d/\mu_c$, as shown in Fig. 4. The minimum diameter of the droplets (43.61 μm) generated in our experiments was limited by the throat size (47.58 μm) at the droplet generating junction. The coefficient of

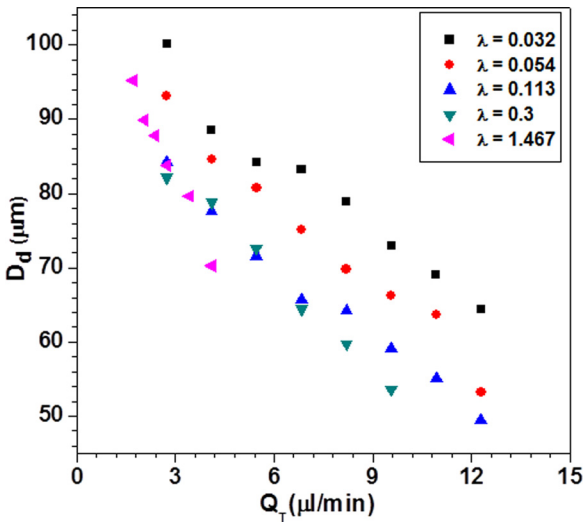

FIG. 4. Effect of total flow rate Q_T on droplet diameter D_d for different viscosity ratios λ.

variation (ratio of standard deviation of the measured values to the mean of the measured values) of droplet diameters and the interdistance between the droplets was measured from repeated experiments, which was found to be less than 3%. Also, in our experiments, the interaction between the droplets can be ignored as the separation distance between them is more than the channel dimension. It was observed that, for a fixed total flow rate, the diameter of the droplets is reduced with increase in the viscosity ratio λ. In our experiments, for high viscosity ratio (e.g., for $\lambda = 1.467$), the minimum size of the droplet generated is restricted by the flow rate because it becomes difficult to produce droplets of uniform size and with equal interdistance between them at higher flow rates. Anna *et al.*[45] reported similar behaviour of decrease in droplet diameter with increase in total flow rate. However, in their work, the effect of viscosity contrast on droplet diameter was not studied. Cubaud and Mason[46] reported the effect of viscosity contrast on diameter of droplet formed which showed a decrease in droplet diameter with increase in viscosity ratio. However, their experiments were carried out without the use of surfactants (which is required for stable droplet formation as per our observations). Adzima and Velankar[15] reported similar observation using T-junction without considering the effect of viscosity contrast at high Ca (2–35), whereas our studies are limited to low Ca (from 0.01 to 0.2).

We studied the effect of droplet size or corresponding Capillary number $Ca = \mu_c U_c/\sigma$ (at fixed viscosity ratio) and viscosity ratio (at fixed droplet size ratio or Ca) on the droplet deformation. Here, σ is the interfacial tension between two phases. At low viscosity ratio (i.e., water droplet with $\lambda = 0.032$), the droplet deformation was observed only for diameter ratio $\rho > 0.7$. However, at higher viscosity ratios (i.e., with 80% glycerol, $\lambda = 1.467$), the droplets were deformed for diameter ratio $\rho > 0.5$. This is in agreement with observations reported in literature,[19,25,47,48] although these studies were carried out for much bigger droplets in larger capillaries and channels. The effect of droplet size ratio $\rho = R_d/R_c$ or Ca (for a fixed viscosity ratio) and viscosity ratio $\lambda = \mu_d/\mu_c$ (for fixed size ratio or Ca) on the deformed shape of the droplets (which indicates deformability) are depicted in Fig. 5. In order to study the effect of droplet size ratio ρ or Ca on droplet deformation (at a fixed viscosity ratio λ) and the effect of viscosity ratio λ on droplet deformation (at fixed droplet size ratio ρ or Ca), we varied the total flow rate Q_T by adjusting both continuous phase flow rate Q_c and discrete phase flow rate Q_d, but the flow rate ratio Q_c/Q_d was not kept fixed. The results show that both droplet size (or Ca) and viscosity have significant influence on the deformability of the droplets. The deformation of the droplets is quantified in terms of deformability index (D.I.), which is defined in Fig. 6(a). The value of D.I. is 0 for undeformed droplets and its value increases as the droplets gets more and more deformed. The variation of D.I. with the droplet size ratio ρ for different values of viscosity ratios λ is presented in Fig. 6(b). At a fixed droplet size ratio (or corresponding fixed Ca), the deformability index is higher for a higher viscosity ratio. Also, for a fixed viscosity

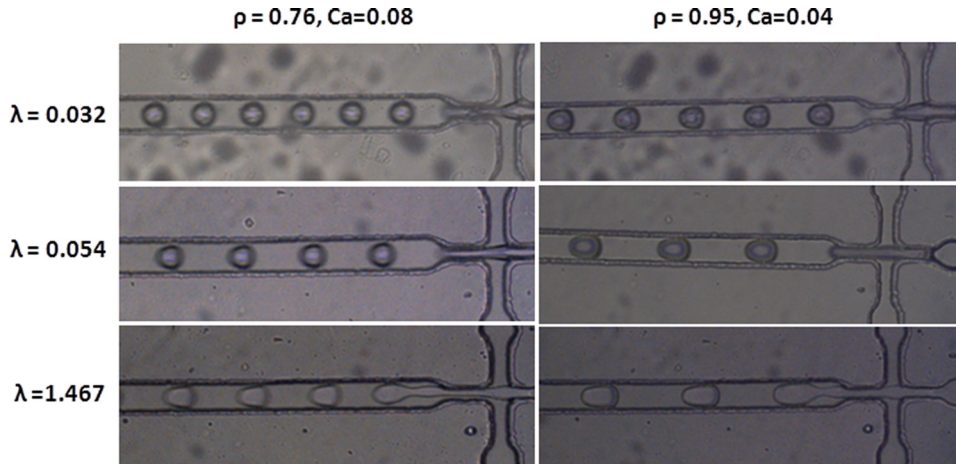

FIG. 5. Images showing the effects of the size ratio ρ (fixed λ) and viscosity ratio λ (fixed ρ) on droplet deformation.

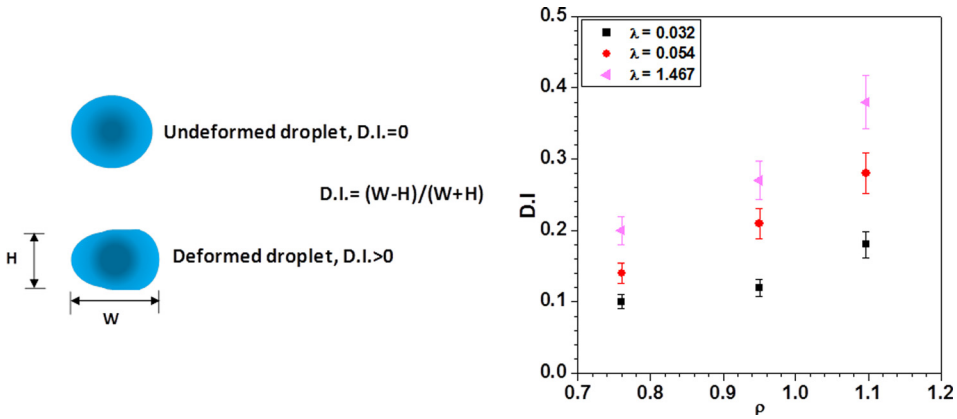

FIG. 6. Definition of D.I. (left) and variation of D.I. with droplet size ratio ρ for different λ (right).

ratio, the deformability index is higher for a higher droplet size ratio (or corresponding higher Ca). Similar observations are reported by Ho and Leal[47] and Martinez and Udell[25] from experimental and numerical works, respectively, but such investigations were carried out for droplets in millifluidic channels.

The droplet generation processes observed from the experiments and predicted from numerical simulations are presented in Fig. 7(a), which compare very well both qualitatively and quantitatively. Under the same operating conditions ($Q_c = 10.5$ and $Q_d = 1.8\ \mu$l/min), the diameters of the droplets measured from the experiments and simulations are 43.61 and 40 μm, respectively. Similarly, the corresponding interdistance between the droplets from the experiments and simulations are 89.69 and 90.90 μm, respectively. The simulation results in terms of droplet size and interdistance match with the corresponding experimental results within 8%. The deformation contours of the droplets of different size ratio ρ and viscosity ratio λ predicted by the model and measured from the experiments are depicted in Fig. 7(b). A very good match between the deformation profiles is observed. For quantitative comparison, the deformations predicted by the simulation and measured from experiments are compared in terms of D.I. The D.I. values from the experimental images and simulations are presented in Fig. 7(b), which match with each other within 5%. In numerical simulations of droplet generation, improper wall boundary condition is one of the critical reasons for deviation of numerical predictions from experimental data. In our simulations, the average static contact angle (which is measured by analysis of droplet formation images obtained from experiments) is given as the wall boundary condition. This improves the match between the simulation and experimental results.

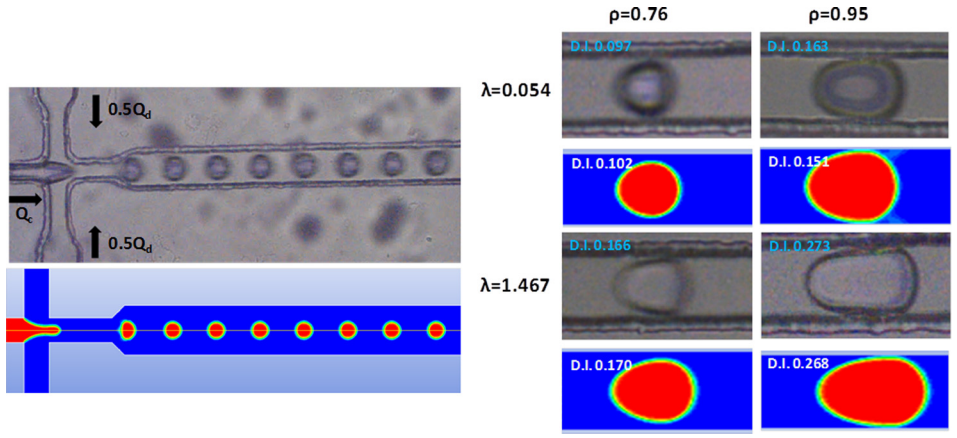

FIG. 7. Comparison between experimental and simulation results: (a) droplet generation process for a water droplets in oil ($Q_c = 10.5$ and $Q_d = 1.8\mu$l/min, contact angle 147°), (b) droplet deformation for different size (ρ) and viscosity (λ) ratios.

Moreover, in our simulations, there is no mass loss problem at the droplet interface during the droplet formation as reported by Lan *et al.*[49] Vigneaux[34] reported the need of a pseudo-3D model in order to capture the surface tension effect in a level set method for the droplet formation. Here, the use of the inbuilt Brackbill surface tension model[33] in Fluent provides the required instability for the droplet formation. Li *et al.*[36] took a similar approach for simulating droplet formation using a flow focusing design but their studies did not include the effect of size ratio and viscosity ratio on droplet deformation.

B. Permeability: Analytical model

We use our experimental data to develop an expression for the permeability k_d of the region around the droplet (refer Eq. (5)) in terms of droplet size ratio ρ and viscosity ratio λ. In the past, many attempts[22,50,51] have been made to establish an analogy between the Darcy's law and Hagen-Poiseuille law for a porous medium using permeability of the medium. The experimentally measured pressure drop data include different flow field conditions that can be divided into three different categories, viz., modified flow field by an undeformed droplets at low values of ρ and λ, modified flow field by a deformed droplet due to wall effect at high values of ρ and low values of λ (and vice versa), and modified flow field by highly deformed droplet due to combined wall effect and high viscosity ratio. The effect of the presence of droplets on the above flow modifications can be accounted for using permeability of the medium k_d. For each individual experimental pressure drop data, the value of the permeability is determined in terms of the droplet diameter ratio ρ and viscosity ratio λ (for 20%–80% glycerol, $\lambda = 0.054 - 1.467$) using the analogy between Darcy and Hagen-Poiseuille equations. The dimensionless permeability (k_d/R_c^2) is correlated with ρ and λ using curve fitting of the data in MATLAB with R^2 value of 0.95 and 95% confidence bound as $k_d^* = \frac{k_d}{R_c^2} = a + b\lambda + c\rho$, where $a = 0.1933$, $b = -0.01559$, and $c = -0.126$.

C. Droplet mobility

From our experimental data, we identified results showing the effects of droplet size ratio ρ (at fixed Ca and λ), and Ca (at fixed ρ and λ), viscosity ratio λ (at fixed ρ and Ca) on the droplet mobility as shown in Fig. 8(a). Keeping viscosity ratio and Ca fixed, the droplet mobility decreases with increase in the droplet size ratio. It is known that the maximum velocity of an undisturbed single phase Poiseuille flow at the centreline of a rectangular microchannel is more than the average flow velocity. So, theoretically, small droplets that are confined to the centreline of the microchannel will move with a higher velocity than the average velocity but lower than the maximum centreline velocity. Our experimental observations for droplet

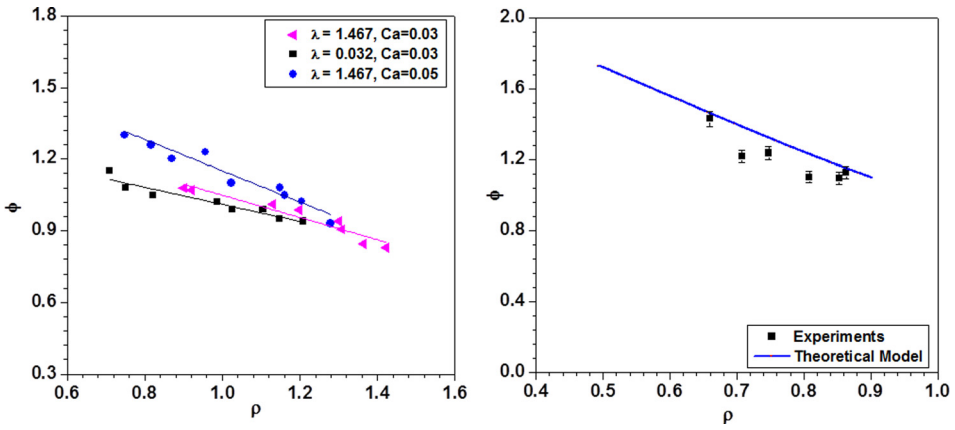

FIG. 8. (a) Variation of droplet mobility ϕ with droplet size ratio ρ for different values of Ca and viscosity ratio λ. (b) Comparison of droplet mobility ϕ predicted from the analytical model and obtained from experimental results with respect to droplet size ratio ρ and viscosity ratio $\lambda = 0.032$.

mobility are in agreement with what is expected theoretically. Additionally, as the wall effects become predominant for larger droplets, the bulk of the data shows a decrease in droplet mobility with increase in droplet size ratio, for all viscosity ratios and Ca. At a fixed Ca and ρ, as the viscosity ratio increases, the mobility increases due to reduced wall effect and increased deformation of the droplets. Finally, for a fixed viscosity ratio and size ratio, as the Ca increases (by varying the flow rate ratio of continuous phase to discrete phase), the droplet mobility increases due to increased deformation of droplet at higher shear rate. The Capillary number Ca was increased by increasing the continuous phase flow rate Q_c. However, in order to keep the droplet size ratio ρ and viscosity ratio λ fixed, the discrete phase flow rate Q_d was also adjusted simultaneously (if the discrete phase flow rate is not adjusted then a higher continuous phase flow rate leads to the formation of smaller droplets). For the range of ρ, Ca, and λ considered in our studies, the droplet mobility varies between 0.8 and 1.3. According to Hetsroni's theoretical model,[24] the maximum possible value of droplet mobility (ϕ) of a small undeformed droplet is 2.0. Our results in terms of the droplet mobility are in agreement with related works reported in literature. Labrot *et al.*[19] and Vanapalli *et al.*[17] investigated mobility of large droplets (liquid plugs) and reported a constant value of mobility of 1.28 and 1.6, respectively. Recently, Sessom *et al.*[22] reported effect of size ratio on mobility for small periodic droplet trains in a cylindrical microfluidic channel but they did not consider the effect of viscosity ratio and Ca on the droplet mobility, which we address in detail. Our experiments are performed with droplets of size ratio $\rho = 0.5 - 1.3$ with Ca in the range 0.01–0.2.

The variation of droplet mobility with the droplet size ratio ρ for a viscosity ratio $\lambda = 0.032$ obtained from experiments and predicted by our theoretical model (presented in Sec. II) are depicted in Fig. 8(b). As shown, the model predictions are in agreement with the experimental data (within 15%). At such low viscosity ratio, the droplets are spherical in shape (not cylindrical). However, our theoretical model assumes a cylindrical droplet moving inside a channel for deriving the expression for velocity in the annular region between the droplet and the channel walls. The deviation of the theoretical model from the experimental data is attributed to this assumption used in the theoretical model. At higher viscosity ratios (e.g., $\lambda = 1.467$), the shape of the droplets is cylindrical; thus, it is observed that the theoretical predictions very closely match with experimental data (within 10%). For intermediate viscosity ratios ($\lambda = 0.054 - 0.3$), the match is within 10%–15%.

D. Hydrodynamic resistance: Droplets

The presence of droplets in a microchannel flow provides additional hydrodynamic resistance (referred as "induced hydrodynamic resistance") as compared to the flow of only continuous phase at the same total flow rate. This induced hydrodynamic resistance is due to the viscous dissipation inside the thin-film of fluid around the droplets that separates the droplets from the channel wall. The presence of large velocity gradients in the thin-film region leads to this viscous dissipation. Additionally, the formation of vortices inside and outside the droplets is also responsible for this additional hydrodynamic resistance.[52–54] The effect of droplet size ratio ρ on the induced hydrodynamic resistance ΔR_d of a single droplet (non-dimensionalised by the hydrodynamic resistance R of the channel with continuous phase only) for different viscosity ratio λ is presented in Fig. 9. It is observed that the induced hydrodynamic resistance $\Delta R_d/R$ increases with increase in the size ratio ρ (following a power law as explained later), for all viscosity ratios λ.

Our experimental data show that the induced hydrodynamic resistance $\Delta R_d/R$ offered by droplets is negligible for smaller droplets with size ratio up to $\rho = 0.6$. In case of medium sized droplets with size ratio $0.6 < \rho < 0.9$, the droplets start to deform and due to the viscous dissipation in the thin film around the droplet and formation of eddies,[52–54] a gradual increase in $\Delta R_d/R$ is observed with increase in the size ratio ρ. In case of large droplets with $\rho > 0.9$, the droplets undergo large deformations and the thickness of thin film around the droplets remains unchanged and become independent of the size ratio ρ. Therefore, as volume of the droplets increases, only the length of thin film increases which leads to a sharp increase in $\Delta R_d/R$ due

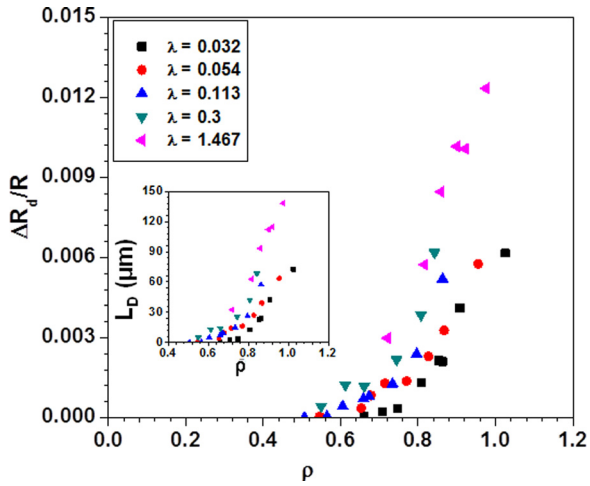

FIG. 9. Effect of droplet size ratio ρ on induced hydrodynamic resistance ($\Delta R_d/R$) for different viscosity ratios λ, effect of ρ on L_d is also shown as inset.

to increased viscous dissipation in the film. The value of induced hydrodynamic length L_d for droplets with viscosity ratio $\lambda < 1$ is less than the droplet diameter (irrespective of the size ratio), whereas the L_d value of the droplets with $\lambda > 1$ and $\rho > 0.9$ are greater than the droplet diameter, as shown in Fig. 9 (inset).

As observed from Fig. 9, at higher droplet size ratios $\rho > 0.9$, the induced hydrodynamic resistance of droplets with viscosity ratio $\lambda > 1$ is much higher as compared to that of droplets with viscosity ratio $\lambda < 1$. For larger droplets, when the viscosity of the droplet is more than the viscosity of continuous phase ($\lambda > 1$), two large vortices are formed at the centre of the droplet due to the contributions from the wall-fluid friction rather than the fluid-fluid friction at the interface,[52–54] which is responsible for such higher induced hydrodynamic resistance. For larger droplets (higher ρ) and higher viscosity ratios λ, the coupled effects of the thin film as well as the vortices are realized due to which the slope of the curve ($\Delta R_d/R$ vs. λ) increases rapidly (curve becomes steeper). The effect of viscosity ratio λ (fixed droplet size ratio ρ) and droplet size ratio ρ (fixed viscosity ratio λ) on the induced hydrodynamic resistance is shown in Fig. 10. It is observed that the induced hydrodynamic resistance $\Delta R_d/R$ increases with increase in the viscosity ratios λ (following a power law as explained later), for all size ratios ρ. The effect of Capillary number Ca on the induced hydrodynamic resistance $\Delta R_d/R$ is depicted in Fig. 11. It is observed that the induced hydrodynamic resistance $\Delta R_d/R$ decreases with an

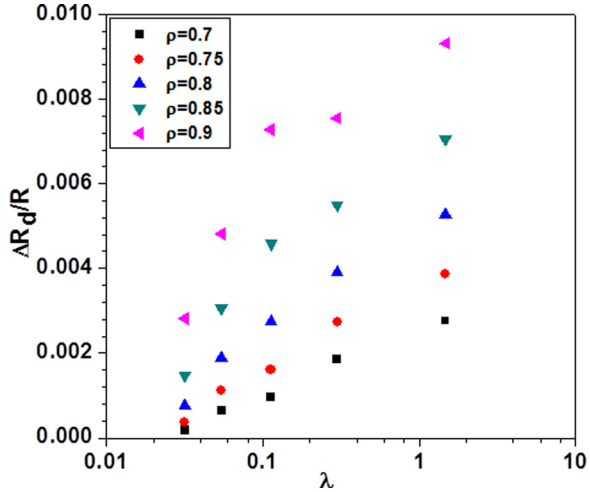

FIG. 10. Effect of viscosity ratio λ on induced hydrodynamic resistance $\Delta R_d/R$ for different droplet size ratio ρ.

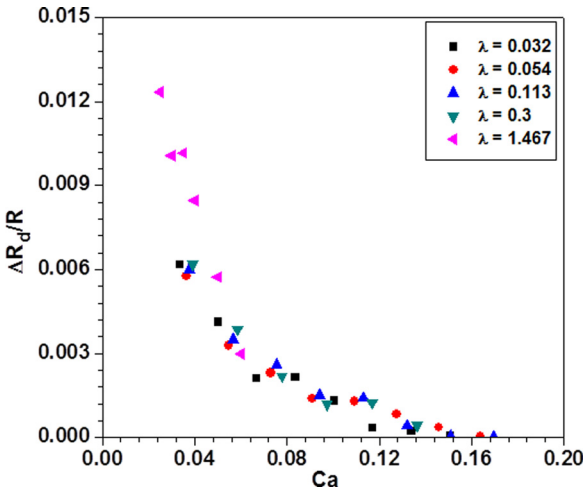

FIG. 11. Effect of Ca on induced hydrodynamic resistance $\Delta R_d/R$ for different viscosity ratio λ.

increase in Ca, irrespective of the viscosity ratios. For $Ca > 0.04$, the variation of induced hydrodynamic resistance with Ca is independent of the viscosity ratios. However, for $Ca < 0.04$, the induced hydrodynamic resistance of droplets of viscosity ratio $\lambda = 1.467$ is found to be much higher than other viscosity ratios.

A comparison between the induced hydrodynamic resistance of droplets $(\lambda = 0.032)$ predicted by our analytical model and measured in our experiments is presented in Fig. 12. The induced hydrodynamic resistance predicted from our analytical model match well with that obtained from the experimental data within a maximum error of 20% (at $\rho = 0.95$). This error can be attributed to the assumption used in the analytical model that flow in the thin film region around the droplets is analogous to the flow in the annular region of a cylindrical droplet present in a concentric cylindrical channel. The comparison between the model predictions and experimental data improves to 5% for droplets of higher viscosity ratio ($\lambda = 1.46$). At higher viscosity ratios, the droplets become cylindrical in shape due to large deformations and thus our assumption regarding the flow in the thin film region is satisfied.

Based on the results presented in Fig. 9, the non-dimensional induced hydrodynamic resistance $\Delta R_d/R$ is correlated with the droplet size ratio ρ and viscosity ratio λ as follows:

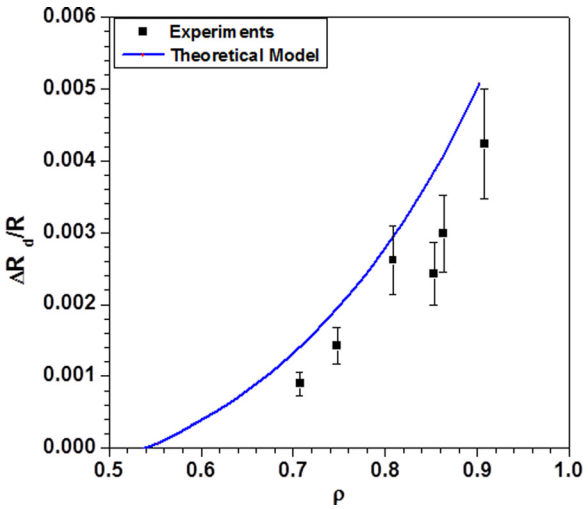

FIG. 12. Comparison of induced hydrodynamic resistance $\Delta R_d/R$ predicted from the analytical model and obtained from experimental results with respect to droplet size ratio ρ and viscosity ratio $\lambda = 0.032$.

$$\frac{\Delta R_d}{R} = A(\lambda)^m(\rho)^n + B, \tag{22}$$

where $A = 0.01439$, $m = 0.2158$, $n = 3.589$, and $B = -0.001259$. This correlation was found by curve fitting of a large set of experimental data in MATLAB with R^2 value of 0.9728 and 95% confidence bound. Additional pressure drop due to the presence of droplets of in a microchannel has been studied in literature.[15,17,19,22] The effects of droplet size,[22] and size and viscosity ratios of liquid plugs[17,19] have been investigated. However, none of these works provide a correlation that could be used for predicting induced hydrodynamic resistance of a single droplet as a function of droplet size ratio and viscosity ratio, which is given in Eq. (22).

E. Hydrodynamic resistance: Beads and cells

We studied the effect of bead/cell concentration (defined in terms of volume fraction α) on the effective viscosity and induced hydrodynamics resistance of the samples. The sample was infused through the microchannel at a particular flow rate and the corresponding pressure drop across the test section (between the pressure taps) was recorded. The effective viscosity of the bead sample was calculated from the experimentally measured pressure drop using the following equation:[55]

$$\mu_{eff} = \frac{\Delta P_s R_c^4}{28.4 Q_s L}, \tag{23}$$

where Q_s and ΔP_s are the sample flow rate and the corresponding pressure drop, respectively, L is the length of the test section (between pressure taps) and R_c is the channel hydraulic radius. Next, the beads and cells were filtered and centrifuged from the sample to obtain the particle-free medium fluid. The medium fluid was infused into the microchannel at same flow rates Q_m (same as Q_s) and the corresponding pressure drop Δp_m was obtained. The excess pressure drop due to the presence of beads and cells in the sample was determined as $\Delta P_{excess} = \Delta P_s - \Delta P_m$. The induced hydrodynamic resistance due to the presence of the beads and cells in the sample was calculated as

$$\Delta R = \frac{\Delta P_{excess}}{Q_m}. \tag{24}$$

In literature, various models have been reported[56] to determine effective viscosity of samples containing particles. However, most of these models investigate effective viscosity of samples at much higher concentration levels, in the range of 0.1–0.8 ml/ml. In our experiments, we have studied the effective viscosity of bead and cell samples with concentration levels lower than 0.001 ml/ml. Our calculations revealed that the theoretical models reported in literature under predict the effective viscosity of bead/cell samples at such low concentration levels. Thus, we had to perform experiments to measure effective viscosity of the samples instead of using models available in the literature.

Three different cells and polystyrene microbeads were used in the present study. The sizes of the yeast cells, L6 myoblast cells, and HEK 293 cells (shown in Fig. 13) were measured to be $15 \pm 3\,\mu$m, $16 \pm 2\,\mu$m, and $18 \pm 2\,\mu$m, and the polystyrene microbeads had a size of $10\,\mu$m. The effective viscosity of the samples was found to increase with increase in the concentration

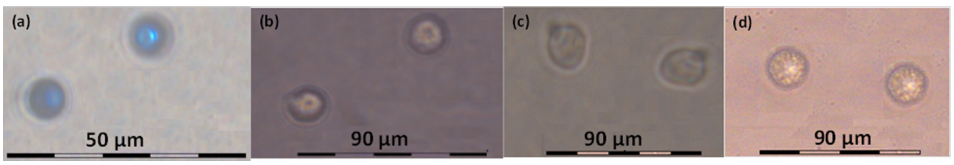

FIG. 13. Images of the (a) Polystyrene beads, (b) L6 cells, (c) yeast cells, and (d) HEK 293 cells.

of bead/ cells as depicted in Fig. 14(a). Although beads are of smaller size as compared to cells at a fixed concentration, the bead sample offers higher effective viscosity than the cell samples. Similarly, it is interesting to observe that although the HEK 293 cells are bigger in size, the HEK 293 sample has lower effective viscosity as compared to the L6 and yeast samples. Also, even though yeast and L6 cells are comparable in terms of their sizes, a large difference (∼20%) between the effective viscosities of the yeast and L6 samples are observed. Thus, effective viscosity could not be directly related to the cell size but may also depend on the cell morphologies including the cell membrane stiffness and deformability of cell cytoplasm, which needs further investigations. Additionally, the particles flowing through a microchannel are focused at some distance away from the wall due to the combined effects of shear induced and wall induced lift forces, thus creating a particle-free fluid layer or a lubrication layer.[29,57,58] For a fixed volume fraction, as the particle size increases, the size of this lubrication layer, which is of the order of the particle size, also increases thus the sample effective viscosity decreases as compared to that for smaller particles. As observed from Fig. 14(a), this effect becomes predominant as the volume fraction of particles α increases.

The effective viscosity of the samples accounts for the volume fraction of the medium and the bead/cells. The effect of bead/cells is represented using a parameter called "apparent viscosity (μ_{app})" such that

$$\mu_{eff} = \alpha\mu_{app} + (1-\alpha)\mu_c, \tag{25}$$

where α is the volume fraction of the bead/cells in the sample by volume. The viscosity of the medium (μ_c) was calculated from the experimental pressure drop data for the medium only and using the Poiseuille equation for a rectangular microchannel. The viscosity of the medium calculated using this method was verified with that measured directly using a Brookfield viscometer which compared very well (within 1%). Thus, this device with the specified pressure tap arrangements and the pressure sensor holds the potential to be used as an on-chip viscometer. From our experimental data, the viscosities of DMEM and YPED media (without cells) were calculated to be 0.000837 and 0.001239 Pa s, respectively. Depending on the volume fraction, the apparent viscosity of beads, yeast cells, L6 cells, and HEK 293 cells were calculated to be in the range of 2– 4.2, 0.2–3.5, 0.15–1.5, and 0.03–0.6 Pa s, respectively.

Next, we study the effect of volume fraction α and the induced hydrodynamic resistance ΔR of different cell populations, as presented in Fig. 14(b). The velocity of bead and cells is lower than that of the medium at the centre of the channel but in the regions closer to the wall, the bead/cells move faster than the medium, which produces an additional hydrodynamic resistance.[29,57,58] The bead/cells present inside the channel undergo uniform translation, rotation, and pure straining motions to modify the flow field and produce higher viscous dissipation. At

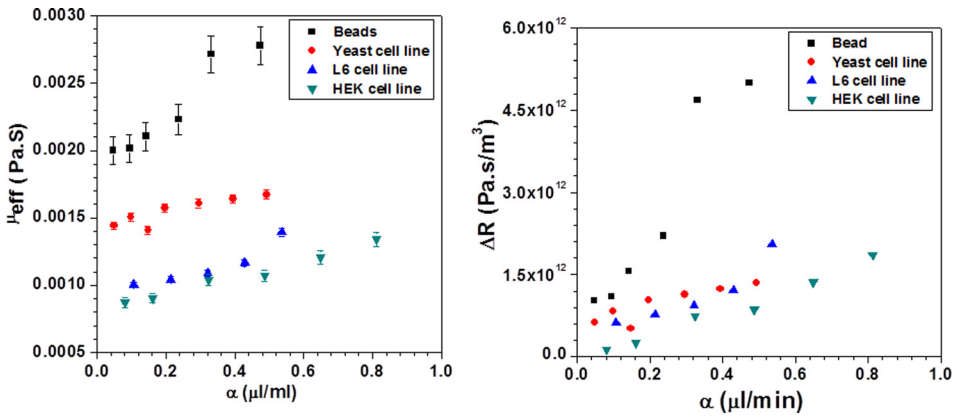

FIG. 14. Effect of bead/cell concentration α on (a) effective viscosity μ_{eff}, (b) induced hydrodynamic resistance, at flow rate 20 μl/min.

higher concentrations, as the number of particles increases, the streamlines become denser and tortuous. Therefore, a higher volume fraction leads to increased effective viscosity of the sample thus higher induced hydrodynamic resistance.

For a fixed volume fraction, the beads provide much higher induced hydrodynamic resistance as compared to the cells which may be due to significantly higher apparent viscosity. Although beads are smaller in size, their stiffness is much higher, which is possibly the reason for higher apparent viscosity and the resulting induced hydrodynamic resistance. Although yeast and L6 cells are of comparable size, yeast cells offer higher induced hydrodynamic resistance, which is due to the higher apparent viscosity of the yeast cells because of different cell morphology (cell membrane of yeast cell is stiffer compared that of L6). As discussed earlier, wall effect plays an important role towards the effective viscosity of cell samples and hence the hydrodynamic resistance. For larger cells, thickness of the cell-free layer (lubrication layer) is higher and thus the effective viscosity and the resulting induced hydrodynamic resistance are lower as compared to that of the smaller cells for the same volume fraction. It is clearly observed that the induced hydrodynamic resistance of the cells is related to their apparent viscosity. The cells of higher apparent viscosity provide higher hydrodynamic resistance, which is also in accordance with the analytical model and experimental results for droplets discussed in Sec. V D. Also, if we compare the slopes of the curves in Figs. 14(a) and 14(b), it is interesting to observe that both effective viscosity and induced hydrodynamic resistance are more sensitive to increase in the volume fraction for beads (stiffer microparticles[59]) as compared to the cells (deformable microparticles). Bulk induced hydrodynamic resistance ΔR ($\mathrm{Pa\,s/m^3}$) offered by the cells in a channel can be correlated with the apparent viscosity μ_{app} (Pa s) and cell concentration α (μl/ml) as follows:

$$\Delta R = A\mu_{app} + B\alpha + C, \tag{26}$$

where $A = 3.452 \times 10^{11}$, $B = 2.19 \times 10^{12}$, and $C = -1.265 \times 10^{11}$. This correlation was found by curve fitting of a large set of experimental data in MATLAB with R^2 value of 0.8824 and 95% confidence bound. The effect of increase in sample concentration on effective viscosity has been reported earlier.[55,60] However, the range of concentration of cells we study in the present work is two orders of magnitude lower as compared to what is reported in the literature. To our knowledge, for the first time, we have related the induced hydrodynamic resistance of living cells with their apparent viscosity and concentration levels in a sample (given in Eq. (26)).

At a fixed bead concentration, as the flow rate of the bead sample increases, the migration effect is enhanced. This leads to reduced local effective viscosity with steep velocity gradient near the channel wall and increased local effective viscosity with mild velocity gradient at the centre.[60] The net result provides a reduced effective viscosity at higher flow rates, which is presented in Fig. 15(a). At higher flow rates, the resulting steep velocity gradient at the wall (thus

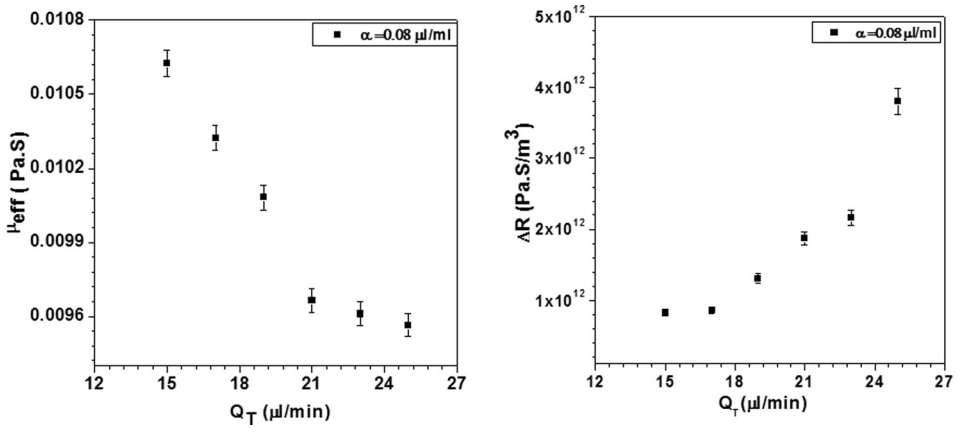

FIG. 15. Effect of flow rate Q_T on (a) effective viscosity μ_{eff} and (b) induced hydrodynamic resistance ΔR.

higher viscous dissipation) leads to an increased wall shear and thus higher hydrodynamic resistance as depicted in Fig. 15(b). Wilding *et al.*[31] reported similar observations, i.e., a decrease in effective viscosity of bio samples and increase in excess pressure drop with increase in the sample flow rate (at fixed concentration) in a silicon microchannel.

VI. CONCLUSION

We have reported experimental and theoretical studies of deformation, mobility ϕ, and induced hydrodynamic resistance $\Delta R_d/R$ of deformable objects such as droplets and cells, and believe our studies would provide important tools and guidelines for design of microfluidic devices for various applications including droplet traffic in microfluidic networks and identification and sorting of biological cells.

We were able to produce droplets of different size ratio by varying the total flow rate Q_T and viscosity ratio λ of the discrete phase. At a fixed total flow rate Q_T, a discrete phase of higher viscosity ratio λ leads to the formation of smaller droplets. Similarly, with the viscosity ratio λ of the discrete phase fixed, a higher total flow rate Q_T generates smaller droplets. We studied the effect of droplet size ratio ρ and viscosity ratio λ on the droplet deformation behaviour. The deformation of droplets was quantified in terms of deformability index, which has a higher value for a more deformable droplet. It was found that the deformability index is higher in the case of droplets of larger size ρ or higher viscosity ratio λ. The effect of droplet size ratio ρ, viscosity ratio λ, and Capillary number Ca on the mobility ϕ of droplets was independently investigated. It was found that for a fixed viscosity ratio λ and Ca, the mobility ϕ of droplets is higher for smaller droplets. At a fixed Ca and size ratio ρ, the mobility ϕ of the droplets increases with increase in the viscosity ratio λ. Finally, for a fixed viscosity ratio λ and size ratio ρ, as the Ca increases (by varying the flow rate ratio of continuous phase to discrete phase), the droplet mobility ϕ also increases. The effect of droplet size ratio ρ and viscosity ratio λ on the induced hydrodynamic resistance $\Delta R_d/R$ was studied. It is observed that the induced hydrodynamic resistance $\Delta R_d/R$ offered by droplets is negligible for smaller droplets with size ratio up to $\rho = 0.6$. In case of medium sized droplets with size ratio increasing in the range $0.6 < \rho < 0.9$, the droplets start to deform, and a gradual increase in $\Delta R_d/R$ is observed. The bigger droplets with $\rho > 0.9$ undergo a fixed deformation in the radial direction but elongate along the flow direction thus their induced hydrodynamic resistance $\Delta R_d/R$ increase rapidly with increase in the size ratio ρ. The effect of Capillary number Ca on the induced hydrodynamic resistance $\Delta R_d/R$ was studied, and it was found that for $Ca > 0.04$, the hydrodynamic resistance is independent of the viscosity ratio λ.

The theoretical model reported here is an extension of the model derived by Sessoms *et al.*,[22] which facilitates experimental measurement of phenomenological permeability which Sessoms *et al.*,[22] does not attempt. Additionally, our model reduces the number of such permeabilities from three to one by (a) considering the flow in the annular region around the droplet and (b) considering the Poiseuille flow profile in the unobstructed region. The proposed theoretical model was validated by comparing the model predictions with experimental results in terms of droplet mobility ϕ and hydrodynamic resistance $\Delta R_d/R$. A good match (within 5%–20%) was found depending on the droplet viscosity ratio λ. Our experiments with different size ratios ρ and viscosity ratios λ indicate that the theoretical model would be applicable to droplets of similar viscosity ratios and microchannels of comparable size. The numerical model accurately predicts the droplet formation process and deformation droplets of different size ratio ρ and viscosity ratio λ. The simulation results in terms of droplet size ρ and interdistance δ and D.I. matched with the corresponding experimental results within 8%. Our experiments with bead and cells revealed that bulk induced hydrodynamic resistance ΔR is related to the bead/cell concentration α and apparent viscosity μ_{app} of the bead/cells. A higher concentration α of bead/cells in a sample provides increased induced hydrodynamic resistance ΔR. At a fixed concentration α of bead/cells, the induced hydrodynamic resistance ΔR is found to be higher for bead/cells with higher apparent viscosity μ_{app}. At a fixed concentration α, as the flow rate Q_T of the bead

sample increases, interestingly the effective viscosity μ_{eff} is reduced but the hydrodynamic resistance ΔR increases.

ACKNOWLEDGMENTS

The authors would like to thank the Department of Biotechnology (DBT), India and Department of Science & Technology (DST), India for providing the financial support for the project. We also acknowledge MEMS Lab of EE, IIT Madras for supporting the photolithography work. The authors thank Dr. R. Vinu, NCCRD, IIT Madras, Dr. M. V. Panchagnula, AM and Dr. A. P. Deshpande, Polymer Engineering and Colloid Science Laboratory, IIT Madras for extending their support for chemical property measurements. The authors also thank Department of Metallurgy for the characterization of channel using SEM. Finally, we acknowledge the help from Dr. V. Geetha and Ms. Y. Rubaiya, Bio Engineering and drug design Lab, IIT Madras for helping us with the cell culture.

[1]A. Manz, D. Harrison, E. M. J. Verpoorte, J. C. Fettinger, A. Paulus, H. Ludi, and H. M. Widmer, J. Chromatogr. **593**, 253 (1992).
[2]G. M. Whitesides and A. D. Stroock, Phys. Today **54**(6), 42 (2001).
[3]M. Toner and D. Irimia, Annu. Rev. Biomed. Eng. **7**, 77 (2005).
[4]P. Bhardwaj, P. Bagdi, and A. K. Sen, Lab Chip **11**(23), 4012 (2011).
[5]G. Goet, T. Baier, S. Hardt, and A. K. Sen, Biomicrofluidics **7**(4), 044103 (2013).
[6]P. Sajeesh and A. K. Sen, Microfluid. Nanofluid. **17**(1), 1 (2013).
[7]J. Voldman, M. L. Gray, and M. A. Schmidt, Annu. Rev. Biomed. Eng. **1**, 401 (1999).
[8]A. K. Sen, J. Darabi, and D. R. Knapp, Sens. Actuators, B **137**(2), 789 (2008).
[9]A. K. Sen, T. Harvey, and J. Clausen, Biomed. Microdevices **13**(4), 705 (2011).
[10]S. Suresh, J. Spatz, J. P. Mills, A. Micoulet, M. Dao, C. T. Lim, M. Beil, and T. Seufferlein, Acta Biomater. **1**(1), 15 (2005).
[11]A. Vaziri and A. Gopinath, Nat. Mater. **7**, 15 (2008).
[12]H. A. Cranston, C. W. Boylan, G. L. Caroll, S. P. Sutera, J. R. Williamson, I. Y. Gluzman, and D. J. Krogstad, Science **223**(4634), 400 (1984).
[13]M. A. C. Ayala and R. Karnik, "Hydrodynamic resistance and sorting of deformable particles in microfluidic circuits," Ph.D. dissertation (MIT University, 2013).
[14]M. S. Raafat, M. C. Ayala, and R. Karnik, in Proceedings of the 14th International Conference on Miniaturized Systems for Chemistry and Life Sciences, The Netherlands, 3–7 October 2010.
[15]B. J. Adzima and S. S. Velankar, J. Micromech. Microeng. **16**, 1504 (2006).
[16]C. N. Baroud, F. Gallaire, and R. Dangla, Lab Chip **10**, 2032 (2010).
[17]S. A. Vanapalli, A. G. Banpurkar, D. V. Ende, M. H. G. Duits, and F. Mugele, Lab Chip **9**, 982 (2009).
[18]W. Engl, M. Roche, A. Colin, P. Panizza, and A. Ajdari, Phys. Rev. Lett. **95**, 208304 (2005).
[19]V. Labrot, M. Schindler, P. Guillot, A. Colin, and M. Joanicot, Biomicrofluidics **3**, 012804 (2009).
[20]Z. He, Z. Dagan, and C. Maldarell, J. Fluid Mech. **222**, 1 (1991).
[21]M. J. Fuerstman, A. Lai, M. E. Thurlow, S. S. Shevkoplyas, H. A. Stone, and G. M. Whiteside, Lab Chip **7**, 1479 (2007).
[22]D. A. Sessoms, M. Belloul, W. Engl, W. M. Roche, L. Courbin, and P. Panizza, Phys. Rev. E **80**, 016317 (2009).
[23]H. Brenner, Ind. Eng. Chem. Fundam. **10**, 537 (1971).
[24]G. Hetsroni, S. Haber, and E. Wacholder, J. Fluid Mech. **41**, 689 (1970).
[25]M. J. Martinez and K. S. Udell, J. Fluid Mech. **210**, 565 (1990).
[26]J. Happel and H. Brenner, *Low Reynolds Number Hydrodynamics* (Prentice-Hall, 1965).
[27]A. Biral and A. Zanella, in *Proceedings of the 3rd IEEE International Workshop on Molecular and Nanoscale Communications (MoNaCom)* (2013), p. 798.
[28]G. L. Goldsmith and S. G. Mason, J. Colloid Sci. **18**, 237 (1963).
[29]G. Segre and A. Silberberg, J. Fluid Mech. **14**, 136 (1962).
[30]M. L. Henle and A. J. Levine, Phys. Fluids **21**, 033106 (2009).
[31]P. Wilding, J. Pfahier, H. H. Bau, J. N. Zemel, and L. J. Kricka, Clin. Chem. **40**(1), 43 (1994).
[32]R. G. Holdich, *Fundamentals of Particle Technology* (Midland Information Technology & Publishing, United Kingdom, 2002).
[33]J. U. Brackbill, D. B. Kothe, and C. Zemach, J. Comput. Phys. **100**, 335 (1992).
[34]P. Vigneaux, "Droplets in microchannels with level set method," in European Conference on Computational Fluid Dynamics ECCOMAS CFD, TU Delft, The Netherlands (2006).
[35]A. M. Leshansky and L. M. Pismen, Phys. Fluids **21**, 023303 (2009).
[36]Y. Li, M. Jain, and K. Nandakumar, "Numerical study of droplet formation inside a microfluidic flow-focusing device," in Excerpt from the Proceedings of the COMSOL Conference, Boston (2012).
[37]D. B. Troy and P. Beringer, *Remington: The Science and Practice of Pharmacy*, 22nd ed. (Lippincott Williams & Wilkins Publisher, USA, 2005).
[38]R. Dreyfus, P. Tabeling, and H. Willaime, Phys. Rev. Lett. **90**(14), 144505 (2003).
[39]Q. Guo, "Surfactants in nonpolar oils: Agents of electric charging and nano-gel templates," Ph.D. thesis (Georgia Institute of Technology, USA, 2012).
[40]L. W. Bergman, "Growth and maintenance of yeast," in *Methods in Molecular Biology, Vol. 177, Two Hybrid Systems* (Humana Press, 2001), p. 9.

[41]V. Nandakumar, V. Geetha, S. Chittaranjan, and M. Doble, Biomed. Pharmacother. **67**(5), 431 (2013).
[42]G. Venkatachalam, V. Nandakumar, G. Suresh, and M. Doble, RSC Adv. **4**(22), 11393 (2014).
[43]S. C. Hur, N. K. Henderson-MacLennan, E. R. B. McCabe, and D. Di Carlo, Lab Chip **11**, 912 (2011).
[44]D. Di Carlo, D. Irimia, R. G. Tompkins, and M. T. Toner, Proc. Natl. Acad. Sci. U.S.A. **104**(48), 18892 (2007).
[45]S. L. Anna, N. Bontoux, and H. A. Stone, Appl. Phys. Lett. **82**(3), 364 (2003).
[46]T. Cubaud and T. G. Mason, Phys. Fluids **20**, 053302 (2008).
[47]B. P. Ho and L. G. Leal, J. Fluid Mech. **71**(2), 361 (1975).
[48]E. Lac and J. D. Sherwood, J. Fluid Mech. **640**, 27 (2009).
[49]W. Lan, S. Li, Y. Wang, and G. Luo, Ind. Eng. Chem. Res. **53**, 4913 (2014).
[50]W. L. Olbricht, Annu. Rev. Fluid Mech. **28**, 187 (1996).
[51]A. E. Scheidegger, *The Physics of Flow Through Porous Media*, 3rd ed. (University of Toronto Press, New York, 1974).
[52]D. Malsch, M. Kielpinski, R. Merthan, J. Albert, G. Mayer, J. M. Kohler, H. S. Sube, M. Stahl, and T. Henkel, Chem. Eng. J. **135S**, 166 (2008).
[53]V. Steijn, M. T. Kreutzer, and C. R. Kleijn, Chem. Eng. Sci. **62**, 7505 (2007).
[54]G. A. Grob, V. Thyagarajan, M. Kielpinski, T. Henkel, and J. M. Kohler, Microfluid. Nanofluid. **5**(2), 281 (2008).
[55]H. Bruus, *Theoretical Microfluidics* (Oxford University Press, United Kingdom, 2008).
[56]A. Einstein, Ann. Phys. **324**, 289 (1906).
[57]M. Poletto and D. D. Joseph, J. Rheol. **39**(2), 323 (1995).
[58]C. Yeh and E. C. Eckstein, Biophys. J. **66**, 1706 (1994).
[59]S. M. Mijailovich, M. Kojic, M. Zivkovic, B. Fabry, and J. J. Fredberg, J. Appl. Physiol. **93**(4), 1429 (2002).
[60]S. H. Cho, H. G. Choi, and J. Y. Yoo, Int. J. Multiphase Flow **31**, 435 (2005).